Check for updates

ADVANCED MATERIALS
www.advmat.de

Moiré Pattern Controlled Phonon Polarizer Based on Twisted Graphene

*Zihao Qin, Lingyun Dai, Man Li, Suixuan Li, Huan Wu, Katherine E. White, Gilad Gani, Paul S. Weiss, and Yongjie Hu**

Twisted van der Waals materials featuring Moiré patterns present new design possibilities and demonstrate unconventional behaviors in electrical, optical, spintronic, and superconducting properties. However, experimental exploration of thermal transport across Moiré patterns has not been as extensive, despite its critical role in nanoelectronics, thermal management, and energy technologies. Here, the first experimental study is conducted on thermal transport across twisted graphene, demonstrating a phonon polarizer concept from the rotational misalignment between stacked layers. The direct thermal and acoustic measurements, structural characterizations, and atomistic modeling, reveal a modulation up to 631% in thermal conductance with various Moiré angles, while maintaining a high acoustic transmission. By comparing experiments with density functional theory and molecular dynamics simulations, mode-dependent phonon transmissions are quantified based on the angle alignment of graphene band structures and attributed to the coupling among flexural phonon modes. The agreement confirms the dominant tuning mechanisms in adjusting phonon transmission from high-frequency thermal modes while having negligible effects on low-frequency acoustic modes near Brillouin zone center. This study offers crucial insights into the fundamental thermal transport in Moiré structures, opening avenues for the invention of quantum thermal devices and new design methodologies based on manipulations of vibrational band structures and phonon spectra.

1. Introduction

Rapid developments have recently been observed in the Moiré patterns of van der Waals structures, offering a new degree of freedom to customize atomic interactions and modify properties that do not occur naturally.[1–5] A prototype example is twisted graphene, which has been the subject of extensive study and groundbreaking discoveries, from superconductivity and ferromagnetism to optical adjustments, photonic responses, and topological transitions.[6–9] To date, most of the efforts have been driven by electronic and optoelectronic features, such as flat bands, strong correlations and interactions, emergent states, and variations in effective mass and density of states. Despite many exciting progress, thermal measurements in twisted graphene remain largely unexplored. In contrast to electrical and optical transport, thermal transport is primarily governed by phonons, i.e., the quantum-mechanical modes of lattice vibrations and their coupling.[10–14] Investigating Moiré pattern mediated thermal transport in twisted graphene provides fundamental insights and new opportunities in controlling heat dissipation and thermal management technologies, while recent advances have been mainly concentrated on computational studies.[15–23] Here, we seek to bridge the gap between experiment and theory and to uncover the complex structure–property relationships of Moiré pattern by detailing the spectral contributions of phonon modes.

Z. Qin, L. Dai, M. Li, S. Li, H. Wu, Y. Hu
Department of Mechanical and Aerospace Engineering
University of California, Los Angeles
Los Angeles, CA 90095, USA
E-mail: yhu@seas.ucla.edu

K. E. White, G. Gani, P. S. Weiss
Department of Chemistry and Biochemistry
University of California, Los Angeles
Los Angeles, CA 90095, USA

The ORCID identification number(s) for the author(s) of this article can be found under https://doi.org/10.1002/adma.202312176

DOI: 10.1002/adma.202312176

K. E. White, G. Gani, P. S. Weiss, Y. Hu
California NanoSystems Institute
University of California, Los Angeles
Los Angeles, CA 90095, USA

P. S. Weiss
Department of Bioengineering
University of California, Los Angeles
Los Angeles, CA 90095, USA

P. S. Weiss, Y. Hu
Department of Materials Science and Engineering
University of California, Los Angeles
Los Angeles, CA 90095, USA

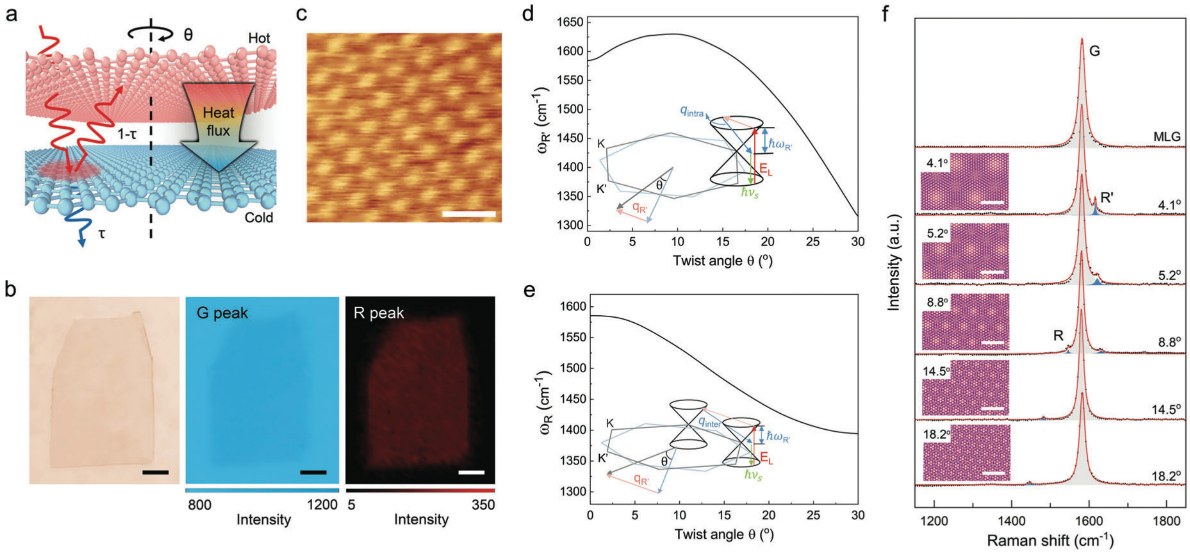

Figure 1. The concept and sample characterizations of phonon polarizer based on twisted graphene. a) Conceptual illustration of twisted graphene phonon polarizer. b) Optical microscope image (left) and Raman spectral mapping of the G (middle) and R (right) peaks of a typical sample. Scale bar, 15 µm. c) Scanning tunneling microscopy (STM) measurement of twisted graphene, showing the Moiré pattern. Scale bar, 15 nm. Plots of the frequency for d) R' and e) R peaks as a function of twist angle, respectively. Inset is the schematic illustration for the physical processes that form the R' (d) and R peaks (e). f) Representative Raman peaks for monolayer graphene and twisted graphene samples with various twist angles. Inset, Moiré patterns of twisted graphene evolving as a function of the twist angles. Scale bar, 2 nm.

In this study, we perform direct experimental measurements on twisted graphene over a wide range of twist angles and observe a marked phonon polarization effect associated with the Moiré pattern. By analyzing experimental data with atomistic theory, we validate the fundamental mechanisms behind the polarization of mode-specific phonon transmission, which stem from the interlayer rotation associated with the Moiré pattern and the resultant breaking of translational symmetry. We further develop quantitative analysis based on first-principles theory to evaluate the phonon band structures and phonon coupling phase space that mediates the interfacial phonon transmission between the two atomic layers as a function of twist angles. Moreover, by conducting concurrent thermal and pico-acoustic measurements, we verify theoretical predictions regarding mode-specific phonon transmission. Our findings indicate that high phonon transmission is preserved for low-frequency acoustic modes, whereas polarized transmission influences high-frequency thermal phonons and the heat flux traversing the Moiré pattern.

2. Concept of Phonon Polarizer and Sample Fabrication

The concept of phonon polarizer, illustrated in **Figure 1**a, is engineered using twisted graphene. Analogous to the case of light transmission where the intensity of the light can be modulated via an optic polarizer by allowing specific vibrations to pass through, here we define a tunable phonon polarizer capable of modulating the interfacial phonon flux, based on the Moiré pattern formed between graphene layers. Microscopically, in this device, when a temperature gradient is applied across the twisted graphene, lattice vibrations are thermally excited to form spectral distributions among all phonon modes while the mode-specific dynamic coupling across the two layers varies subject to the Moiré pattern. The device operates on the principle that as twist angles (θ) vary, the coupling of phonons across the atomic interface induces polarization in the phonon transmission (τ), and thereby governing the energy integration across all phonon modes—that is, the heat flux.

To create the samples, we employed a custom nano-alignment setup (Experimental Section), which involved transferring a monolayer of graphene onto a substrate of graphene to achieve rotational stacking. The twist angle between the top adjacent atomic layers, which determines the heat flux via the modulation of lattice dynamics by the Moiré pattern, is ascertained through Raman spectral characterization. As shown in Figure 1b, the distinct optical reflection contrast enables the identification of the twisted structure with precision down to a single atomic layer using optical imaging. We characterized the unique vibrational modes of the top monolayer graphene and the substrate by their respective G peaks in the Raman spectra (middle, Figure 1b). Notably, the G peak at ≈1580 cm^{-1} is indicative of the in-plane bond stretching of sp^2-bonded carbon atoms.[24] The intensity of this peak, spatially mapped, is utilized to confirm and differentiate the top monolayer from the substrate layer (as seen in the middle of Figure 1b), corroborating the optical contrast observed in the imaging. In addition, to verify the high quality of the samples, we performed scanning tunneling microscopy that directly measured the Moiré patterns of the twisted graphene, as shown in Figure 1c.

The twist angle is determined through the interlayer double-resonance Raman process, which involves the R' and R peaks corresponding to intravalley longitudinal optical and intervalley transverse optical Raman scattering,[25–27] respectively. These peaks have a determined relationship[25] with their characteristic vibrational frequencies ($\omega_{R'}$ and ω_R) that depend on θ, as shown in Figure 1d,e. Due to the different energy requirements for the

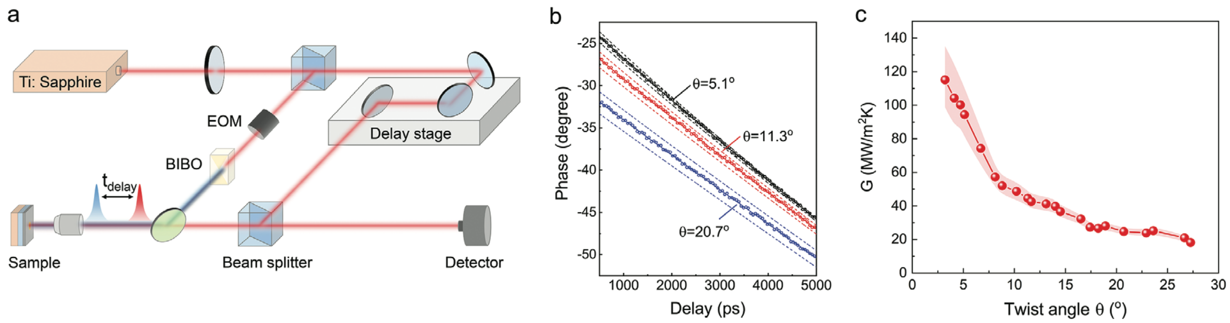

Figure 2. Experimental measurement of thermal transport in Moiré graphene as a function of twist angles. a) Schematic of ultrafast pump–probe optics setups for thermal conductance measurements. b) Representative experimental data: TDTR phase signal versus time for twisted graphene under 5.1° (black circles), 11.3° (red circles), and 20.7° (blue circles), fitted by thermal transport model (solid lines). Dashed lines are calculated curves using thermal conductivity change by ±10% to illustrate measurement accuracy. c) The measured thermal conductance G as a function of twist angle.

R' and R peaks, the R' peak is typically observable at smaller angles (less than 9°), while the R peak is discernible at larger angles. Together, the R' and R peaks provide a comprehensive fingerprint for determining twist angles across the entire spectrum from 0 to 30°. For instance, the R' peak shifts from 1609 cm^{-1} at $\theta = 3.2°$ to 1631 cm^{-1} at 8.8°, while the R peak moves from 1543 cm^{-1} at 8.8° to 1400 cm^{-1} at 27.2° (Figure 1f). As highlighted in the insets of Figure 1f, the Moiré patterns that emerge and evolve with θ are a consequence of the changing twisted lattice structures that in turn progressively alter the phonon band structures, which will be analyzed later in the manuscript.

3. Experimental Measurements of Thermal Resistance as a Function of Twist Angles

We conducted experiments to characterize the heat flux in twisted graphene samples by measuring the interfacial thermal conductance (G), given by the equation:

$$G = \frac{q''}{\Delta T} \tag{1}$$

where q'' represents the areal heat current, and ΔT is the temperature difference between the two atomic layers. We measured G directly using ultrafast optical pump–probe spectroscopy via the time-domain thermoreflectance (TDTR) technique. TDTR is a standard method for measuring the interfacial thermal conductance of various materials, including van der Waals materials.[11,28–31] In our TDTR setup, depicted in **Figure 2**a, a series of femtosecond laser pulses is split into pump and probe beams. The pump beam instantaneously heats the sample's surface, while the probe beam detects the temperature decay on the surface with sub-picosecond time resolution. We determine the thermal conductance by fitting the experimental data to the heat conduction equation, as illustrated in Figure 2b. Further details on the TDTR setup and measurements are available in our recent publications.[11–13,32] As shown in Figure 2c, the measured G as a function of θ displays a remarkable dependency: G is 1.15×10^8 W m^{-2} K^{-1} at $\theta = 3.2°$ and decreases with increasing θ, reaching 1.82×10^7 W m^{-2} K^{-1} at $\theta = 27.2°$. This significant tuning ratio of interfacial thermal conductance, over sixfold, is observed experimentally for the first time and confirms that the interfacial heat flux is strongly modulated in twisted graphene. Compared to the estimated effective thermal conductance in pristine graphite (i.e., converted by cross-plane thermal conductivity over the interlayer distance), the tuning ratio exceeds 820 times for $\theta = 27.2°$.

Fundamentally, G is a cumulative integration over all phonon modes, with mode-specific phonon transmission, $\tau(\nu)$ that describes the probability for the phonons with frequency ν to transport across the interface. Quantitively, G and $\tau(\nu)$ can be related with the Landauer formalism[10]:

$$G = \int_0^\infty M(\nu)\, h\nu\tau(\nu)\, \frac{\partial f_{\mathrm{BE}}}{\partial T} d\nu \tag{2}$$

where ν, f_{BE}, $M(\nu)$ represent phonon frequency, Bose–Einstein distribution function and the number of propagating modes, respectively. h is the Planck's constant. Therefore, we ascribe the tuning of heat flux to the polarized mode-specific phonon transmission τ that controls the phonon transmission probability across the interface of twisted structure. This is due to the Moiré-pattern-induced alterations in phonon band structures, which we further analyze using atomistic and first-principles theory analysis.

We assessed the interfacial thermal transport in twisted graphene by employing molecular dynamics (MD) simulations under steady-state and transient conditions.

4. Modeling Interfacial Heat Flux with Steady-State and Transient Molecular Dynamics

First, for the steady-state MD simulations, we establish a invariant temperature gradient by applying a constant heat flux across the graphene layers.[30] Consequently, G is derived from heat flux and geometric settings with Fourier's law.[17,18,33,34] By analyzing the correlation function of heat flux, we can identify the phonon mode-specific contribution to G. Moreover, we performed transient MD simulations to exclude potential size-effects caused by the ballistic phonon transport near thermal reservoirs. In the transient MD simulations, we apply an ultrafast heat pulse excitation to the top graphene layer, resulting in an instantaneous temperature change, which simulates the dynamics of heat transfer in twisted graphene. The comprehensive evaluations aim to

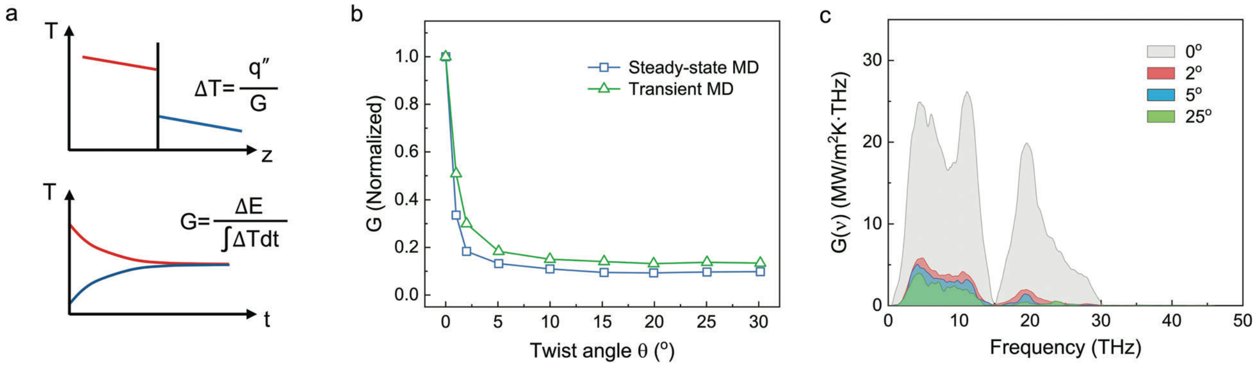

Figure 3. Modeling interfacial heat flux and phonon mode-specific contributions of twisted graphene from molecular dynamics. a) Illustration temperature profiles for steady-state MD (top) and transient MD (bottom) simulations, respectively. b) Normalized simulation results of thermal conductance (G) as a function of twist angle (θ). c) Spectral thermal conductance $G(\nu)$ mediated by mode-specific phonon transmissions in twisted graphene at various angles.

reveal the inherent transport characteristics of twisted interfaces and identify the roles of heat carriers. The two simulation algorithms are respectively through spatial and temporal temperature profiles (**Figure** 3a). Further details about the simulations can be found in the Experimental Section and Supporting Information. The simulation results, displayed in Figure 3b, show consistency between the two MD approaches. The G values experience a pronounced reduction at small range of θ (from 0° to 15°), and then levels off. The observed trend agrees with recent literature studies,[15–23,33,35] and indicates that the variations of atomic arrangements in the Moiré unit cells become less sensitive to layer rotation when θ increases.

To elucidate the role of phonon mode-dependent transmission in influencing interfacial heat flux, we quantify the frequency-dependent spectral thermal conductance, $G(\nu)$, that is dictated by the phonon transmission $\tau(\nu)$ based on Equation (2). The thermal conductance is the cumulative effect of all phonon eigenmodes across a broad spectrum of frequencies, shown as an integration:

$$G = \int G(\nu)\, d\nu \tag{3}$$

We determined $G(\nu)$ by applying a Fourier transform to the velocity–force correlations at the interface based on the data from the steady-state MD.[36] The results of $G(\nu)$ are plotted in Figure 3c, allowing us to look at how θ affects the phonon spectral distributions. From the perfect alignment in pristine graphene ($\theta = 0°$), to a slight misalignment at $\theta = 2°$, we observed a strong decline in $G(\nu)$ across a broad range of phonon frequencies. This suggests that upon the formation of a Moiré pattern at a small twist angle, significant disruption in phonon transmission is introduced by the minor deviation from the perfect alignment and thus the spatially non-uniform interlayer coupling impede the heat propagation over broad phonon spectra. As the twist angle further progresses from 2° to 25°, the resulting Moiré period (i.e., the size of the Moiré unit cell, as detailed in the Supporting Information) continues to change but at a more gradual slope, rendering the reductions in G and $G(\nu)$ less impactful across the phonon spectrum. This is in line with our phonon polarizer design concept, which selectively blocks phonon propagation until it reaches a saturation point at the symmetry angle ($\theta = 30°$), where extreme misalignment occurs. Also, a gap in $G(\nu)$ is observed at around 15 THz, which we attributed to the phonon band gap between the flexural acoustic and optical branches, as discussed with the phonon band structure analysis in **Figure** 4.

5. First-Principles Theory for Polarized Phonon Transmission in Moiré Patterns

To dissect the phonon polarization mechanisms influenced by the Moiré angle, we developed first-principles analysis[37–39] to understand the interfacial phonon transmission. Based on density functional theory, we hypothesize that thermal transport in the twisted structure is mediated through coherent waves established between phonon spectra from one atomic layer and the other. In this scenario, phonons in the two layers can interfere constructively and transmit through the interface, allowing for energy transport via quantum tunneling,[40–42] provided that energy and momentum conservation are satisfied. The magnitude of the coupling phase space[37,38,43]—representing the number of viable transport channels and transition probabilities—is pivotal, forming the tuning principle for our phonon polarizer concept. Consequently, based on the phonon transmission picture, we calculated the angle-dependent phonon band structures that reveal the matching of spectral energy and momentum of the phonons.

Figure 4a displays the phonon band structure for the top monolayer graphene along the reciprocal lattice vector path Γ-K, in reference to the bottom monolayer's lattice coordinate (details in the Experimental Section). In this coordinate, the band structure of the bottom graphene is fixed (i.e., always remains as the curve of 0° in Figure 4a), while that of the top graphene changes with various twist angles. When the two atomic layers are precisely aligned ($\theta = 0°$), their phonon band structures coincide perfectly (black curve). As θ increases, discrepancies between the layers' phonon dispersions emerge, notably within the transverse and longitudinal acoustic branches. For instance, at the K point, the phonon frequency of transverse acoustic modes in top layer graphene is ≈30 THz when layers at $\theta = 0°$, and it reduces to ≈20 THz at $\theta = 30°$. Such angle-dependent phonon band structures dictate the phonon spectral matching between top and bottom graphene layers, and thereby modifying the phonon transmission between the two monolayers.

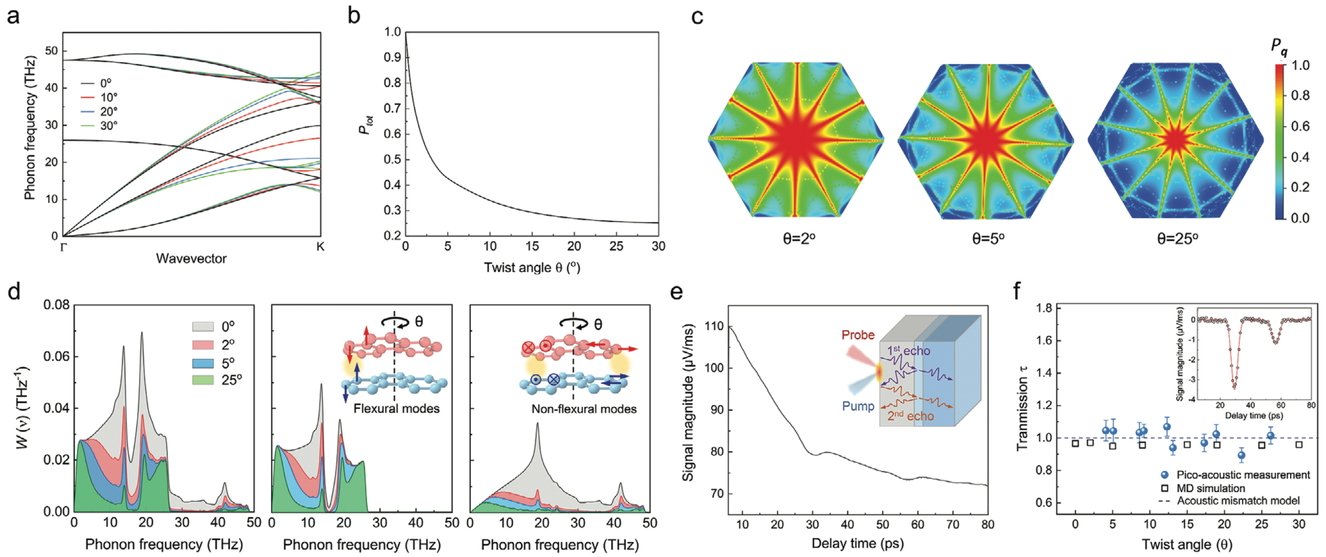

Figure 4. First-principles analysis of the band structure and phonon transmission and acoustic measurements in twisted graphene. a) Angle-dependent phonon dispersion of twisted graphene. b) Normalized phase space P_{tot} as a function of twist angle. c) Reciprocal space-resolved phonon phase space P_{q} for twisted graphene under 2°, 5°, and 25°, respectively. d) Spectral weighted phonon phase space $W(\nu)$ from all polarizations (left), flexural modes (middle), and non-flexural modes (right) for twisted graphene under various angles. Inset, the schematic of corresponding vibrational modes through the twisted interface. e) Pico-acoustic measurements of the transmission of acoustic phonon modes near the center of the Brillouin zone. Inset, schematic of the picosecond acoustic pulse measurements. f) The measured low-frequency acoustic transmission (circles), plotted with the results from MD simulations (squares), and acoustic mismatch model (dashed line), as a function of twist angles. Inset, measurement data after background extraction.

We further quantify the phonon transmission by looking at the coupling phase space across the two monolayers. We define the coupling phase space P_{qs} as the amount of scattering channels available as determined by energy and momentum conservation conditions and thus determines the phonon transmission probability across the two monolayers. Mathematically, we calculate for a phonon mode with wavevector q and polarization s as:

$$P_{\mathrm{qs}} = w \sum_{s'} \delta\left(\omega_{\mathrm{qs}}^{\mathrm{bottom}} - \omega_{\mathrm{qs'}}^{\mathrm{top}}\right) \tag{4}$$

where $\omega_{\mathrm{qs}}^{\mathrm{bottom}}$ and $\omega_{\mathrm{qs'}}^{\mathrm{top}}$ are the frequencies of phonons in the bottom and top graphene, respectively, and $w = 1/\delta(\omega \to 0)$ is a normalization factor for non-dimensionalization. The momentum-specific coupling phase space P_{q} and the total coupling phase space P_{tot} are defined as:

$$P_{\mathrm{q}} = \frac{1}{m} \sum_{\mathrm{s}} P_{\mathrm{qs}} \tag{5}$$

$$P_{\mathrm{tot}} = \frac{1}{N} \sum_{\mathrm{q}} P_{\mathrm{q}} \tag{6}$$

where m represents the number of phonon branches and N is the total count of $\boldsymbol{q}$-points within the first Brillouin zone mesh. As shown in Figure 4b, P_{tot} shows a downward trend from 1.0 to 0.25 as the twist angle expands from 0° to 30°. This trend, resembling the experimental measurements (Figure 2c), unveils a microscopic view wherein a reduction in the available transmission channels with increased θ typifies the observed dependency of thermal transport blockage on the angle. Additionally, Figure 4c illustrates the momentum-resolved phase space P_{q} within the first Brillouin zone for twist angles of 2°, 5°, and 25°, underscoring a diminishing number of transport channels for most phonon modes as misalignment escalates, with significant transmission probabilities concentrated near 12 specific ridges (Figure 4c) due to the intrinsic symmetry of monolayer graphene along the Γ-K and Γ-M paths.

To contextualize the energy carried by each phonon into the coupling phase space, we address the observed curvature of $G(\nu)$ in Figure 3c. Given that the energy varies across different transport channels, we refined our model to include a weighted coupling phase space W_{qs}, defined as:

$$W_{\mathrm{qs}} = \frac{C_{\mathrm{qs}} P_{\mathrm{qs}}}{\frac{1}{N} \sum_{\mathrm{qs}} C_{\mathrm{qs}}} \tag{7}$$

Here, C_{qs} signifies the volumetric specific heat for phonon mode $\boldsymbol{qs}$. Figure 4d presents the spectral contributions to the weighted coupling phase space $W(\nu)$ across phonon frequencies ν for twist angles of 0°, 2°, 5°, and 25°. The profile of $W(\nu)$ aligns with the $G(\nu)$ obtained through MD simulations, as shown in Figure 3c, indicating that both the quantity of available transport channels and the thermal occupation are well-represented in the theoretical framework of phonon transmission physics for twisted graphene.

Separating contributions from flexural (out-of-plane vibrations) and non-flexural (in-plane vibrations) modes, we find that in pristine bilayer graphene ($\theta = 0°$), flexural and non-flexural modes both significantly influence cross-layer transport, with only 58.5% of the phase space stemming from flexural phonons. However, as twisting is introduced, flexural modes become increasingly dominant, accounting for 73.4% of the phase space at a twist angle θ of 2° and reaching up to 82.2% at $\theta = 25°$. This finding indicates that the minimum in $G(\nu)$ at 15 THz is mirrored by a corresponding minimum in $W(\nu)$ for flexural modes, a phenomenon arising from the energy bandgap between the flexural acoustic and optical modes, as shown in Figure 4a. Moreover, the result further elucidates the implications and operation principles of the phonon polarizer: introducing Moiré pattern significantly hinders the transport pathways for non-flexural phonon modes while preferentially allowing flexural modes to conduct varying amounts of heat, with the efficiency of heat transport being influenced by the degree of stacking commensurability.

6. The Conservation of High Phonon Transmission for Acoustic Propagations

Remarkably, while the modeling results presented in Figure 4c suggest that the interfacial transmission in twisted graphene is heavily influenced by the twist angle, an exception was observed at the zone center: The low-frequency modes that are responsible for acoustic wave propagation, maintain high transmission regardless of θ. This theory predicts that low-frequency acoustic phonons consistently demonstrate high transmission across the twist interface for any given twist angle. To experimentally validate this model prediction, we conducted picosecond laser ultrasonic measurements[2,31] aimed at directly examining acoustic transmission across the twisted graphene interface, as shown in Figure 4e. The working principle of picosecond laser ultrasonic technique[12,31] is illustrated in the inset of Figure 4e: A pump laser generated a picosecond acoustic wave that traversed the sample at the speed of sound. Upon reaching the top graphene interface, the wave was partly reflected, resulting in the creation of primary and secondary sound echoes. These echoes were subsequently detected by the probe laser upon their return to the surface, which enabled the measurement of the echo intensity. The intensity ratio of the second to the first echoes, I_2/I_1, following background extraction, is employed to analyze low-frequency phonon transmission. As compiled in Figure 4f, the pico-acoustic experiments (circles) show consistently high acoustic transmission at the graphene interface across all twist angles, corroborating the findings from MD simulations (squares). This revelation confirms that twisting does not significantly affect the transmission of acoustic waves, thereby substantiating the constancy of the Γ point phase space at unity for various angles. Under the simplification for acoustic wave propagation, the observation also concurs with the classical acoustic mismatch model,[44] which postulates that there should be no acoustic impedance for two identical material layers when the sole variable is their relative orientation (dashed line). Contrastingly, the high-frequency phonons, which dominate heat transfer, are strongly modulated in moiré patterns due to the polarization of interfacial phonon transmission that vary with the twist angles.

7. Summary

In summary, we have successfully demonstrated a phonon polarizer within Moiré systems with the first thermal measurements across twisted graphene. Our ultrafast pump–probe spectroscopy measurements disclosed that the thermal conductance could be modulated by up to 631% as twist angles varied from 3.2° to 27.2°, due to strong tuning by the Moiré pattern over the phonon transmission of high-frequency thermal phonons. By contrast, our modeling and pico-acoustic experiments reveal that the acoustic transmission remained consistently high for low-frequency phonons near the Brillouin zone center. This remarkable thermal regulation was ascribed to selective mode polarization of interface transmission across a phonon spectrum spanning from 0 to 30 THz. In addition, we performed atomistic modeling and first-principles calculations to provide quantitative analysis on the mode-dependent phonon transport across twisted structures, revealing a decrease in phonon transmission and consequently weaker phonon–phonon couplings with increased twist angles, as quantified by the coupling phase space. Notably, flexural modes were identified as the major contributors to cross-layer transport in the twisted architecture, accounting for 73% of the weighted phase space at a twist angle of 2° and rising to dominate over 82% at 25°. This study not only propels our quantitative understanding of the microscopic mechanisms of energy transport in twisted van der Waals heterojunction systems but also offers crucial insights for the strategic design of innovative materials.

8. Experimental Section

Fabrication of Twisted Graphene Samples: Monolayer graphene was grown on copper substrate via chemical vapor deposition. Few-layer graphene was mechanically exfoliated from Bernal-stacked highly oriented pyrolytic graphite and served as the graphene substrate. The twisted graphene samples were prepared by transferring one monolayer graphene onto the graphene substrate. To form rotational stacking, a transfer method was developed using a customized nano-alignment setup. The monolayer graphene on copper substrate was attached to PDMS film, which was prepared using the SYLGARD 184 silicone elastomer kits. After gentle placement, conformal contact between the graphene and the PDMS film was accomplished and PDMS was stamped onto a glass slide. Copper was etched with a 0.4 M ammonium persulfate solution. After rinsing with DI water to remove the etchant residue, the PDMS/graphene was pressed gently onto the multilayer graphene substrate. After the peel-off process, twisted graphene samples can be observed clearly with optical characterizations (Figure 1b).

Raman Spectroscopy: A high-resolution confocal micro-Raman system (inVia, Renishaw) equipped with a motorized sample stage was used for the measurement of Raman spectra and two-dimensional spatial mapping. To satisfy the energy requirements for the R' and R peaks, two lasers with different wavelength: $\lambda = 488$ and 633 nm, and a 1200 mm^{-1} grating were used for laser excitation. The laser has a backscattering geometry with a Leica DM2500 optical system. A × 50/0.75 objective lens was used to provide a lateral spatial resolution < 0.5 µm.

Time-Domain Thermoreflectance Technique for Thermal Measurements: The time-domain thermoreflectance (TDTR) technique is a non-contact optical method widely used for thermal conductivity measurement. In the setup, a mode-locked Ti:sapphire laser with 80 MHz repetition rate generates ultrafast laser pulses and splits into pump and probe beams. The probe beam is fixed at 800 nm while the pump beam frequency is doubled to 400 nm by a second harmonic generator. The pump pulse is absorbed by the sample and results in an instantaneous temperature rise. The probe beam monitors the sample temperature with a controlled time delay in reference to the pump beam using a mechanical delay stage. The time-dependent temperature measurements are fitted with thermal model and allow the extraction of thermal conductance. More details regarding TDTR and thermal conductance measurement can be found in the recent papers.[11–13,28–32,45,46]

Picosecond Acoustic Pulse Technique for Acoustic Measurements: In the picosecond acoustic pulse setup, a femtosecond pump pulse beam was used to generate a longitudinal acoustic wave propagating from the surface into the sample at the speed of sound. When the acoustic wave reached the sample interface, it was partially reflected and created sound echoes when returning to the surface, which were then detected by a femtosecond probe beam. A mechanical delay stage was used to allow sub-picosecond time resolution for detecting the wave propagation and time interval between the sound echoes, which determines the speed of sound with precision. More details regarding the pico-acoustic experimental setup and measurement can be found in the recent papers.[12,31]

Molecular Dynamics Simulations: The molecular dynamics (MD) simulations in this work were performed using Large-scale Atomic/Molecular Massively Parallel Simulator (LAMMPS) package. AB-stacked graphene systems with various twist angles were generated following the method reported in the literature.[17,47–51] The initial intralayer carbon–carbon bond length was set to 1.42 Å whereas the interlayer distance was set to 3.35 Å. The strong in-plane covalent bonding was modeled using the reactive empirical bond-order potential while the weak cross-plane van der Waals bonding was modeled using the state-of-the-art interlayer potential, which was tested to generate more accurate graphene phonon dispersion to experimental data than the typical Leonard–Jones potentials. Two types of MD simulations, i.e., steady-state MD and transient MD, were employed. The timestep of 0.5 fs was used in all the simulations.

In transient MD simulations, the systems were composed of bilayer-twisted graphene. The systems first experienced relaxation in the isothermal-isobaric (NPT) ensemble at a temperature of 270 K and zero pressure for 200 ps, followed by a 200 ps canonical ensemble (NVT) stage and another 200 ps microcanonical ensemble (NVE) stage. Then, the temperature of the top layer was rescaled to 330 K for 50 fs, simulating an ultrafast heat pulse imposed on the top layer, simultaneously the bottom layer remained unchanged. The temperature difference between the two layers resulted in thermal energy exchange, which in the end, led to a quasi-steady-state where both the two layers achieved the same temperature of 300 K. The temperature evolution of such a transient process was recorded and further used to extract the interfacial thermal conductance of this bilayer twist interface, based on the instantaneous energy conservation equation.[52,53]

In steady-state MD simulations, the systems in this study were 8-layer AB stacked, which were essentially 4-layer graphene on another 4-layer graphene with a twisted interface occurring between the 4th and 5th layers. After equilibration in an NPT ensemble at a temperature of $T = 300$ K and zero pressure for 250 ps, a 1.5 ns simulation with fixed boundary conditions at two ends was carried out as a production run, where the steady-state data of the last 500 ps was used to extract thermal conductance. Specifically, in the simulation, a specified heat flux was added to and extracted from the layers next to the two ends of the system, and the resulting steady-state temperature drop at the twisted interface was used to calculate interfacial thermal conductance based on Fourier's law.[30,54] The heat flux was chosen so that the entire temperature drop across the system is less than 30 K to avoid nonlinear effects.

Phonon Mode Specific Decomposition of Thermal Conductance: Frequency-domain spectral decomposition of thermal conductance was obtained using Fourier's transforming velocity–force correlations on steady-state MD data every 10 time steps for 1.5 ns, according to the following equation[36,55]:

$$G(\omega) = \frac{2}{A\Delta T} Re \sum_{i\in\{UI\}} \sum_{i\in\{LI\}} \int_{-\infty}^{\infty} d\tau \, e^{i\omega\tau} \left\langle \boldsymbol{F}_{ij}(\tau) \cdot \boldsymbol{v}_i(0) \right\rangle \tag{8}$$

where ω is the angular frequency of vibration, A is cross-section area, ΔT is the temperature drop at the twisted interface, UI stands for upper interface region within interlayer force cutoff radius to the twisted interface, LI stands for lower interface region within interlayer force cutoff radius to the twisted interface, τ is the correlation time between forces and velocities, $\boldsymbol{F}_{ij}$ is the atomic force on atom i due to atom j, $\boldsymbol{v}_i$ is the velocity of atom i. Since the classical statistics in MD can overestimate the phonon contribution spectrum, quantum correction was applied to every frequency, where the heat capacity of each mode was rescaled to the one consistent with the Bose–Einstein distribution. The obtained corrected spectral conductance was then re-integrated for extraction of total thermal conductance, as reported in Figure 3b.

Acoustic Wave Transmission Simulation: Acoustic wave transmission simulation was done at 0 K in two-end fixed multilayer systems. Similar to the wave-packet method,[56] by applying initial displacement to the top layer and recording subsequent atomic velocities and positions of the systems, the transmission was determined by calculating the ratio of the wave energy before and after crossing the twist interface.

First-Principles Calculations: First-principles calculations in this work were performed invoking Density Functional Theory (DFT) as implemented in the Quantum Espresso package.[57–60] The vdW-DF-ob86 pseudopotential was used. The kinetic energy cutoff was 120 Ry. The lattice constant of graphene was obtained by minimizing the total energy of the system in the ground state using 24 × 24 × 1 Monkhorst–Pack mesh. The second-order force constants were calculated by fitting atomic forces and displacements based on a 24 × 24 × 1 supercell with 2 × 2 × 1 Monkhorst–Pack mesh using the ALAMODE package.[60] Then the obtained force constants were used to calculate dispersion relations by diagonalizing dynamical matrices. The coupling phase space was calculated following the recent reports[37,38] and the procedure developed in this work.

Supporting Information

Supporting Information is available from the Wiley Online Library or from the author.

Acknowledgements

Z.Q., L.D., M.L., and S.L. contributed equally to this work. Y.H. acknowledges support from the National Science Foundation under Grant No. DMR-1753393, an Alfred P. Sloan Research Fellowship under Grant No. FG-2019–11788, and a NIGMS Research Award under Grant No. R35GM147391. K.E.W., G.G., and P.S.W. acknowledge support from NSF CHE-2004238. For this paper, the authors used computational and storage services associated with the Hoffman 2 Shared Cluster provided by UCLA Office of Advanced Research Computing's Research Technology Group, and the Bridges-2 at Pittsburgh Supercomputing Center through Allocation No. DMR180111 from Advanced Cyberinfrastructure Coordination Ecosystem: Services & Support.

Conflict of Interest

The authors declare no conflict of interest.

Data Availability Statement

The data that support the findings of this study are available in the Supporting Information of this article.

Keywords

interfacial thermal conductance, Moiré pattern, phonons, thermal conductivity, thermal management, thermal transport, twisted graphene

Received: November 14, 2023
Revised: February 23, 2024
Published online: March 26, 2024

[1] A. K. Geim, I. V. Grigorieva, *Nature* **2013**, *499*, 419.
[2] K. S. Novoselov, A. Mishchenko, A. Carvalho, A. H. Castro Neto, *Science* **2016**, *353*, 9439.
[3] E. Pomerantseva, Y. Gogotsi, *Nat. Energy* **2017**, *2*, 17089.
[4] S. Carr, S. Fang, E. Kaxiras, *Nat. Rev. Mater.* **2020**, *5*, 748.
[5] B. Zhao, Z. Wan, Y. Liu, J. Xu, X. Yang, D. Shen, Z. Zhang, C. Guo, Q. Qian, J. Li, R. Wu, Z. Lin, X. Yan, B. Li, Z. Zhang, H. Ma, B. Li, X. Chen, Y. Qiao, I. Shakir, Z. Almutairi, F. Wei, Y. Zhang, X. Pan, Y. Huang, Y. Ping, X. Duan, X. Duan, *Nature* **2021**, *591*, 385.
[6] Y. Cao, V. Fatemi, S. Fang, K. Watanabe, T. Taniguchi, E. Kaxiras, P. Jarillo-Herrero, *Nature* **2018**, *556*, 43.
[7] A. L. Sharpe, E. J. Fox, A. W. Barnard, J. Finney, K. Watanabe, T. Taniguchi, M. A. Kastner, D. Goldhaber-Gordon, *Science* **2019**, *365*, 605.
[8] X. Liu, Z. Hao, E. Khalaf, J. Y. Lee, Y. Ronen, H. Yoo, D. Haei Najafabadi, K. Watanabe, T. Taniguchi, A. Vishwanath, P. Kim, *Nature* **2020**, *583*, 221.
[9] M. He, Y. Li, J. Cai, Y. Liu, K. Watanabe, T. Taniguchi, X. Xu, M. Yankowitz, *Nat. Phys.* **2021**, *17*, 26.
[10] Y. Cui, M. Li, Y. Hu, *J. Mater. Chem. C* **2020**, *8*, 10568.
[11] M. Li, H. Wu, E. M. Avery, Z. Qin, D. P. Goronzy, H. D. Nguyen, T. Liu, P. S. Weiss, Y. Hu, *Science* **2023**, *382*, 585.
[12] S. Li, Z. Qin, H. Wu, M. Li, M. Kunz, A. Alatas, A. Kavner, Y. Hu, *Nature* **2022**, *612*, 459.
[13] J. S. Kang, M. Li, H. Wu, H. Nguyen, Y. Hu, *Science* **2018**, *361*, 575.
[14] L. Lindsay, D. A. Broido, N. Mingo, *Phys. Rev. B* **2010**, *82*, 115427.
[15] W. Ren, S. Lu, C. Yu, J. He, Z. Zhang, J. Chen, G. Zhang, *Appl. Phys. Rev.* **2023**, *10*, 41404.
[16] W. Ren, Y. Ouyang, P. Jiang, C. Yu, J. He, J. Chen, *Nano Lett.* **2021**, *21*, 2634.
[17] W. Ouyang, H. Qin, M. Urbakh, O. Hod, *Nano Lett.* **2020**, *20*, 7513.
[18] X. Nie, L. Zhao, S. Deng, Y. Zhang, Z. Du, *Int. J. Heat Mass Transfer* **2019**, *137*, 161.
[19] M.-H. Wang, Y.-E. Xie, Y.-P. Chen, *Chin. Phys. B* **2017**, *26*, 116503.
[20] Y. Cheng, Z. Fan, T. Zhang, M. Nomura, S. Volz, G. Zhu, B. Li, S. Xiong, *Mater. Today Phys.* **2023**, *35*, 101093.
[21] W. Liu, Y. Wu, Y. Hong, B. Hou, J. Zhang, Y. Yue, *Phys. Chem. Chem. Phys.* **2021**, *23*, 19166.
[22] W. Sun, S. Xue, J. Jiang, *Comput. Mater. Sci.* **2023**, *229*, 112436.
[23] W. Liu, Y. Hong, J. Zhang, Y. Yue, *Phys. Chem. Chem. Phys.* **2022**, *24*, 21722.
[24] A. C. Ferrari, J. C. Meyer, V. Scardaci, C. Casiraghi, M. Lazzeri, F. Mauri, S. Piscanec, D. Jiang, K. S. Novoselov, S. Roth, A. K. Geim, *Phys. Rev. Lett.* **2006**, *97*, 187401.
[25] V. Carozo, C. M. Almeida, E. H. M. Ferreira, L. G. Cançado, C. A. Achete, A. Jorio, *Nano Lett.* **2011**, *11*, 4527.
[26] C.-C. Lu, Y.-C. Lin, Z. Liu, C.-H. Yeh, K. Suenaga, P.-W. Chiu, *ACS Nano.* **2013**, *7*, 2587.
[27] J.-B. Wu, X. Zhang, M. Ijäs, W.-P. Han, X.-F. Qiao, X.-L. Li, D.-S. Jiang, A. C. Ferrari, P.-H. Tan, *Nat. Commun.* **2014**, *5*, 5309.
[28] J. S. Kang, M. Ke, Y. Hu, *Nano Lett.* **2017**, *17*, 1431.
[29] M. Li, J. S. Kang, Y. Hu, *Rev. Sci. Instrum.* **2018**, *89*, 84901.
[30] M. Li, J. S. Kang, H. D. Nguyen, H. Wu, T. Aoki, Y. Hu, *Adv. Mater.* **2019**, *31*, 1901021.
[31] J. S. Kang, H. Wu, M. Li, Y. Hu, *Nano Lett.* **2019**, *19*, 4941.
[32] J. S. Kang, M. Li, H. Wu, H. Nguyen, T. Aoki, Y. Hu, *Nat. Electron.* **2021**, *4*, 416.
[33] L. Zhang, Y. Zhong, X. Li, J.-H. Park, Q. Song, L. Li, L. Guo, J. Kong, G. Chen, *Nano Lett.* **2023**, *23*, 7790.
[34] W. Jiang, T. Liang, J. Xu, W. Ouyang, *Int. J. Heat Mass Transfer* **2023**, *217*, 124662.
[35] F. Eriksson, E. Fransson, C. Linderälv, Z. Fan, P. Erhart, *ACS Nano.* **2023**, *17*, 25565.
[36] K. Sääskilahti, J. Oksanen, J. Tulkki, S. Volz, *Phys. Rev. B* **2014**, *90*, 134312.
[37] H. Fan, H. Wu, L. Lindsay, Y. Hu, *Phys. Rev. B* **2019**, *100*, 85420.
[38] H. Wu, H. Fan, Y. Hu, *Phys. Rev. B* **2021**, *103*, L041203.
[39] H. Wu, Z. Qin, S. Li, L. Lindsay, Y. Hu, *Phys. Rev. B* **2023**, *108*, L140302.
[40] M. Prunnila, J. Meltaus, *Phys. Rev. Lett.* **2010**, *105*, 125501.
[41] I. Altfeder, A. A. Voevodin, A. K. Roy, *Phys. Rev. Lett.* **2010**, *105*, 166101.
[42] B. K. Ridley, *Phys. Rev. B* **1994**, *49*, 17253.
[43] L. Lindsay, D. A. Broido, *J. Phys.: Condens. Matter* **2008**, *20*, 165209.
[44] R. E. Peterson, A. C. Anderson, *Phys. Lett. A* **1972**, *40*, 317.
[45] J. S. Kang, H. Wu, Y. Hu, *Nano Lett.* **2017**, *17*, 7507.
[46] Y. Hu, L. Zeng, A. J. Minnich, M. S. Dresselhaus, G. Chen, *Nat. Nanotechnol.* **2015**, *10*, 701.
[47] A. P. Thompson, H. M. Aktulga, R. Berger, D. S. Bolintineanu, W. M. Brown, P. S. Crozier, P. J. in 't Veld, A. Kohlmeyer, S. G. Moore, T. D. Nguyen, R. Shan, M. J. Stevens, J. Tranchida, C. Trott, S. J. Plimpton, *Comput. Phys. Commun.* **2022**, *271*, 108171.
[48] N. N. T. Nam, M. Koshino, *Phys. Rev. B* **2017**, *96*, 75311.
[49] D. W. Brenner, O. A. Shenderova, J. A. Harrison, S. J. Stuart, B. Ni, S. B. Sinnott, *J. Phys.: Condens. Matter.* **2002**, *14*, 783.
[50] W. Ouyang, I. Azuri, D. Mandelli, A. Tkatchenko, L. Kronik, M. Urbakh, O. Hod, *J. Chem. Theory Comput.* **2020**, *16*, 666.
[51] E. J. Mele, *Phys. Rev. B* **2010**, *81*, 161405.
[52] J. Zhang, Y. Hong, Y. Yue, *J. Appl. Phys.* **2015**, *117*, 134307.
[53] Z.-Y. Ong, E. Pop, *Phys. Rev. B* **2010**, *81*, 155408.
[54] A. J. H. McGaughey, M. Kaviany, in *Advances in Heat Transfer* (Eds: G. A. Greene, J. P. Hartnett, A. Bar-Cohen, Y. I. Cho), Elsevier, New York **2006**, pp. 169–255.
[55] K. Sääskilahti, J. Oksanen, S. Volz, J. Tulkki, *Phys. Rev. B* **2015**, *91*, 115426.
[56] P. K. Schelling, S. R. Phillpot, P. Keblinski, *Appl. Phys. Lett.* **2002**, *80*, 2484.
[57] P. Giannozzi, S. Baroni, N. Bonini, M. Calandra, R. Car, C. Cavazzoni, D. Ceresoli, G. L. Chiarotti, M. Cococcioni, I. Dabo, A. Dal Corso, S. de Gironcoli, S. Fabris, G. Fratesi, R. Gebauer, U. Gerstmann, C. Gougoussis, A. Kokalj, M. Lazzeri, L. Martin-Samos, N. Marzari, F. Mauri, R. Mazzarello, S. Paolini, A. Pasquarello, L. Paulatto, C. Sbraccia, S. Scandolo, G. Sclauzero, A. P. Seitsonen, et al., *J. Phys.: Condens. Matter.* **2009**, *21*, 395502.
[58] J. Klimeš, D. R. Bowler, A. Michaelides, *Phys. Rev. B* **2011**, *83*, 195131.
[59] P. Wisesa, K. A. McGill, T. Mueller, *Phys. Rev. B* **2016**, *93*, 155109.
[60] T. Tadano, Y. Gohda, S. Tsuneyuki, *J. Phys.: Condens. Matter* **2014**, *26*, 225402.